

Charting the Landscape of Oxygen Ion Conductors: A 60-Year Dataset with Interpretable Regression Models

*Seong-Hoon Jang^{*1}, Shin Kiyohara¹, Hitoshi Takamura², Yu Kumagai^{**1,3}*

¹ *Institute for Materials Research, Tohoku University, 2-1-1 Katahira, Aoba-ku, Sendai 980-8577, Japan.*

² *Department of Materials Science, Graduate School of Engineering, Tohoku University, 6-6-02 Aramaki, Aoba-ku, Sendai 980-8579, Japan.*

³ *Organization for Advanced Studies, Tohoku University, 2-1-1 Katahira, Aoba-ku, Sendai 980-8577, Japan*

*Corresponding authors:

jang.seonghoon.b4@tohoku.ac.jp (S.-H. Jang)

yukumagai@tohoku.ac.jp (Y. Kumagai)

ABSTRACT

Oxygen ion conductors are indispensable materials for such as solid oxide fuel cells, sensors, and membranes. Despite extensive research across diverse structural families, systematic data enabling comparative analysis remain scarce. Here, we present a curated dataset of oxygen ion conductors compiled from 84 experimental reports spanning 60 years, covering 483 materials. Each record includes activation energy (E_a) and prefactor (A) derived from Arrhenius plots, alongside detailed metadata on structure, composition, measurement method, and data source. When the original papers derive these using an erroneous Arrhenius equation $\sigma_T = A \exp\left(-\frac{E_a}{RT}\right)$, where (σ_T is the oxygen ion conductivity at temperature T and R is the gas constant), we replotted these using the correct one, $\sigma_T T = A \exp\left(-\frac{E_a}{RT}\right)$. To illustrate how the database can be used, we constructed interpretable regression models for predicting oxygen ionic conductivity. Two symbolic regression models for E_a and A suggest that oxygen ion transport is primarily governed by local coordination environment and the electrostatic interactions, respectively. This dataset establishes a reliable foundation for data-driven discovery and predictive modeling of next-generation oxygen ion conductors.

KEYWORDS. Oxygen ion conductors, materials database, symbolic regression, structure-property relationships, ionic conductivity

Background & Summary

Oxygen ion conductors are key functional materials underpinning technologies such as solid oxide fuel cells, oxygen sensors, and catalytic membranes, where efficient ionic transport is essential for performance and sustainability.¹⁻⁸ Over the past six decades, a wide range of structural families, including perovskites/fluorites family,⁹⁻⁴⁵ Bi-based family (such as δ -Bi₂O₃,^{41, 46-54} BIMEVOX,⁵⁵⁻⁵⁹ and Bi₂UO₆ classes⁶⁰), complex framework family (such as scheelite,⁶¹⁻⁷² apatite,⁷³⁻⁸¹ cuspidine,⁸²⁻⁸⁴ melilite,⁸⁵⁻⁸⁸ garnet,^{89, 90} pyrochlore,⁹¹ and columbite classes⁹²) and α -SrSiO₃ family,⁹³⁻⁹⁶ have been reported to exhibit oxygen ion conductivity. Recent breakthroughs in Ba₄Nb₄MoO₂₀⁻ and α -SrSiO₃-based materials highlight the promise of structural diversity in enabling fast ion transport.^{36, 96} However, the richness of these material families also poses a challenge: the structural and chemical space remains sparsely explored, and systematic design principles for new conductors are limited.

To address this gap, comprehensive data collection and curation are essential. Here, we present a manually curated dataset of oxygen ion conductors derived from 84 experimental reports, encompassing 483 unique oxides published over 60 years.^{10-39, 41, 43-96} The dataset provides activation energies (E_a) and prefactors (A) extracted from Arrhenius-type analyses of ionic conductivity. When the original papers fit the conductivity using an erroneous Nernst-Einstein formula, we replot the conductivity and reevaluated these (see **Methods**). To examine the effectiveness of our database, we constructed interpretable two symbolic regression models that predict E_a and A . These models enable the identification of dominant descriptors and offering physical insights into the factors governing oxygen ion transport. This dataset not only consolidates the historical knowledge base but also offers a foundation for data-driven discovery and design of next-generation oxygen ion conductors. In addition, our systematic data will be utilized for the validation of machine learning potentials, which have been developing rapidly in recent years.⁹⁷⁻⁹⁹

Methods

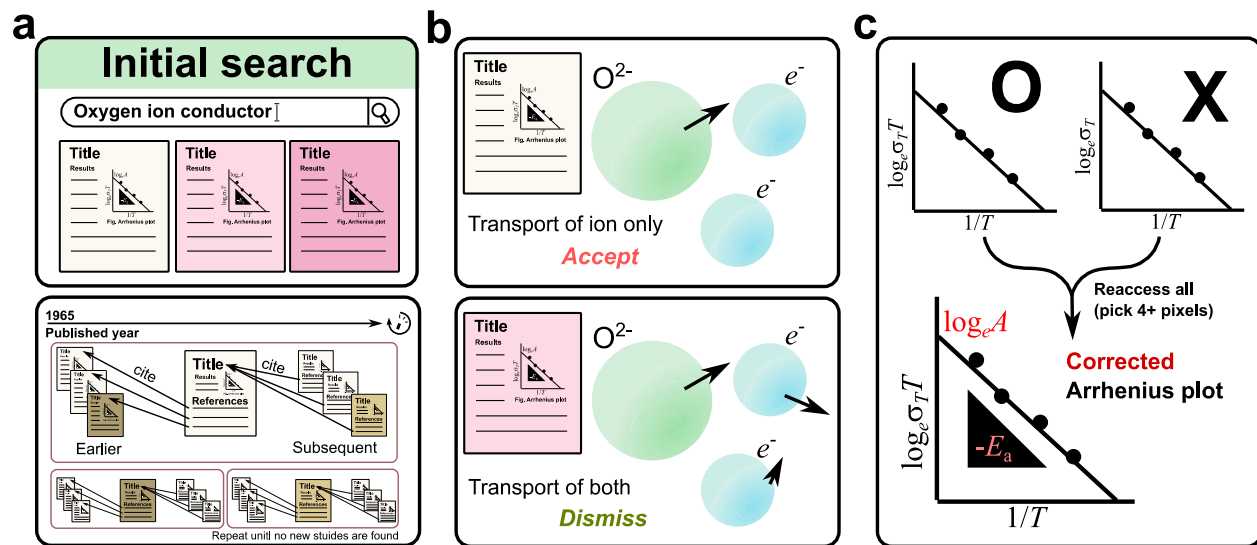


Fig. 1 Workflow for dataset construction and curation of oxygen ion conductors. (a) Initial literature search using multiple academic databases identified candidate reports containing multi-temperature oxygen ion conductivities. Forward and backward citation searches were then performed iteratively until no additional relevant studies were found. (b) Conductivities dominated by electronic contributions were excluded to ensure that the dataset represents oxygen ion transport. (c) To correct for the widespread use of an incorrect Nernst-Einstein equation, all reported plots were manually re-examined (see text for details). For example, activation energies (E_a) and prefactors (A) were recalculated from at least four data points in figures to eliminate systematic biases and ensure consistency across the dataset.

To construct a comprehensive dataset of oxygen ion conductors, we systematically surveyed the literature spanning the past 60 years (Fig. 1a). We first used multiple academic search engines including Web of Science,¹⁰⁰ Scopus,¹⁰¹ and Google Scholar¹⁰² with keywords such as “oxygen ion conductivity”, “Arrhenius plots”, and “solid oxide fuel cells”. From the identified reports containing oxygen ion conductivities at multiple temperatures (σ_T , where T are measured temperatures), we then expanded our search by following two directions: (i) backward citations (references cited by these papers) and (ii) forward citations (subsequent papers citing them). This iterative process was repeated until no new experimental studies with relevant conductivity data

were found. In this study, we targeted both purely oxygen ion conducting electrolytes and mixed ionic-electronic conductors; in the latter case, only the data in which the oxygen-ion conductivity was explicitly separated from the electronic contribution were included,^{11, 12, 22, 31} and all others were excluded (**Fig. 1b**). Note that such mixed ionic–electronic conductors may include additional inaccuracies due to methodological assumptions/uncertainties in deriving oxygen-ion diffusivities.

A common issue in the literature is the use of an incorrect form of the Arrhenius plots. The correct form of Arrhenius equation is $\sigma_T T = A \exp\left(-\frac{E_a}{RT}\right)$, which is derived from $\sigma_T T = D_T \frac{cq}{k_B}$ and the Nernst-Einstein equation $D_T = A_D \exp\left(-\frac{E_a}{RT}\right)$, where R , D_T , c , q , k_B , and A_D denote the gas constant, the self-diffusion coefficient, the density of charge carriers, the ionic charge, the Boltzmann constant, and the prefactor for A_D , respectively). However, many reports instead erroneously use $\sigma_T = A \exp\left(-\frac{E_a}{RT}\right)$. This inconsistency results in systematic errors in E_a and A . To address this, all conductivity plots were carefully re-examined (**Fig. 1c**); an example is provided in the **Supplementary Information**. For figures, at least four points were manually extracted across the measured temperature range; for tables, a minimum of two data points were used. From these, E_a and A were recalculated to ensure consistency across the dataset. This labor-intensive manual curation is the most important contribution of this study, which allowed us to standardize parameters and eliminate inherited biases.

Data Records

The dataset comprises oxygen ion conductivity parameters extracted from 84 experimental reports spanning 60 years, covering 483 oxides. Each entry in the dataset corresponds to one oxide under a given measurement condition and includes E_a and A derived from the Arrhenius plots. For cases where the Nernst-Einstein relationship exhibits two distinct linear regions, both the low-temperature ($T < T^*$) and high-temperature ($T > T^*$) regimes are reported separately, with the break point temperature (T^*) explicitly recorded. To ensure consistency and reproducibility, each data entry is annotated with extensive metadata (**Table 1**).

Table 1 Metadata fields for the curated dataset.

Field	Description
References	Family name of the first author, journal title, volume, initial page number, and published year.
DOI	Digital Object Identifier of the source publication, enabling traceability.
Year	Publication year of the experimental report.
Class	Structural class of the material (e.g., perovskite, scheelite, apatite).
Formula	Reported chemical composition.
Parsed formula	Standardized composition represented by $A_s-B_s(-C_s)$ site classification. For example, in the perovskite oxide $\text{La}_{0.95}\text{Sr}_{0.05}\text{Ga}_{0.95}\text{Mg}_{0.05}\text{O}_{3-\delta}$, La and Sr occupy the A_s -site, while Ga and Mg occupy the B_s -site of the perovskite lattice. ¹⁰
E_a / A	Activation energy in meV and prefactor in $\text{K} \cdot \text{S} \cdot \text{cm}^{-1}$. When there are two distinct linear regions, values for the low-temperature regime are shown.

$E_{a,HT} / A_{HT}$	Activation energy and prefactor values for the high-temperature regime (if applicable).
T^*	Transition temperature separating low- and high-temperature regimes (if applicable).
Type of σ_T	Conductivity type, distinguishing bulk conductivity from total conductivity (bulk and grain boundary contributions).
Measurement	Experimental technique employed (e.g., two-probe AC, impedance spectroscopy).
Measurement temperature range	The range of temperatures over which experimental measurements were performed.
Source	Origin of the data within the publication (figure or table reference).
Plot type	Axis configuration used in the original Arrhenius representation (e.g., $\log_e \sigma_T$ - $1000/T$)

Data Statics

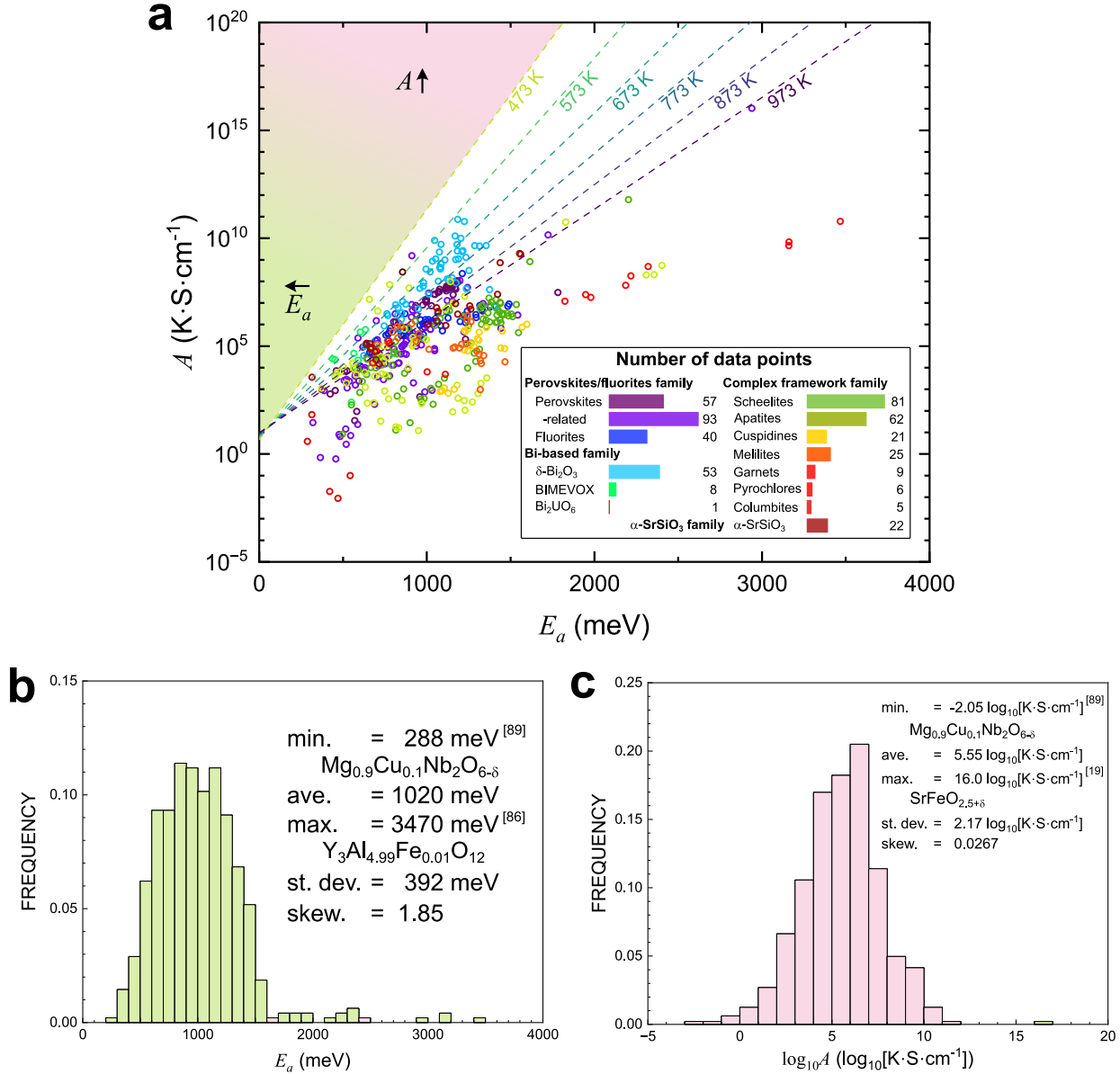


Fig. 2 Overview of the curated dataset of oxygen ion conductivities. (a) Distribution of activation energy (E_a) and prefactor (A) for 483 oxides. We show A in the low-temperature regime when two-region behavior was reported. Dashed lines indicate the condition required to achieve oxygen ionic conductivity $\sigma_T \geq 10^{-2} \text{ S}\cdot\text{cm}^{-1}$ at different temperatures ($T = 473 - 873 \text{ K}$). The shaded region ($T < 473 \text{ K}$) highlights the particularly challenging region, which may be accessed either by suppressing E_a (pink) or enhancing A (green). The inset shows the classification of the dataset into 14 structural classes, along with the corresponding number of entries in each class. (b, c)

Histograms of (b) E_a and (c) $\log_{10} A$. In (b) and (c), statistical parameters (minimum, average, maximum, standard deviation, and skewness) are provided; for minima and maxima, the experimental reports with their formula are referred to.^{20, 89, 92}

Fig. 2a illustrates the distribution of data points across all oxides in the A - E_a domain. For visualization, we used the low-temperature regime ($T < T^*$) when two-region behavior was reported. Dashed guidelines indicate the condition to achieve $\sigma_T \geq 10^{-2} \text{ S} \cdot \text{cm}^{-1}$ at different temperatures. Notably, none of the investigated materials surpass this threshold at 473 K, underscoring the persistent challenge of achieving high ionic conductivity at intermediate temperatures. Access to this regime may be achieved either by reducing E_a (pink-shaded region) or by increasing A (green-shaded region). However, the weak positive correlation between E_a and A complicates this effort, underscoring the need to decouple descriptors for E_a and A in order to guide efficient materials design. Based on our dataset, the most effective oxygen ion conductors exhibiting $\sigma_T \geq 10^{-2} \text{ S} \cdot \text{cm}^{-1}$ for $T = 473 - 573 \text{ K}$ are α -SrSiO₃-type Sr_{1.65}Na_{1.35}Si₃O_{8.325} ($E_a = 315 \text{ meV}$ and $A = 3.59 \times 10^3 \text{ K} \cdot \text{S} \cdot \text{cm}^{-1}$),⁹⁵ apatite-type Nd_{9.5}Si_{5.5}Al_{0.5}O₂₆ ($E_a = 658 \text{ meV}$ and $A = 1.45 \times 10^7 \text{ K} \cdot \text{S} \cdot \text{cm}^{-1}$) and Nd_{9.83}Si_{4.5}Al_{1.5}O₂₆ ($E_a = 779 \text{ meV}$ and $A = 7.05 \times 10^7 \text{ K} \cdot \text{S} \cdot \text{cm}^{-1}$),⁷⁹ Bi₂UO₆ ($E_a = 856 \text{ meV}$ and $A = 2.69 \times 10^8 \text{ K} \cdot \text{S} \cdot \text{cm}^{-1}$),⁶⁰ and BIMEVOX-type Bi₂V_{0.9}Mg_{0.1}O_{5.35} ($E_a = 911 \text{ meV}$ and $A = 1.54 \times 10^9 \text{ K} \cdot \text{S} \cdot \text{cm}^{-1}$).⁹³

The oxides in the dataset are classified into 14 structural classes, namely perovskite, perovskite-related, fluorite, δ -Bi₂O₃, BIMEVOX, Bi₂UO₆, scheelite, apatite, cuspidine, melilite, garnet, pyrochlore, columbite, and α -SrSiO₃ classes. The counts of oxides per class are shown in the inset of **Fig. 2a**. Perovskites and related compounds constitute the largest fraction of reported data, reflecting the dominant research focus in the field, followed by scheelites, apatites, and other structures.

Fig. 2b shows the distribution of E_a , with most values lying between 200 and 2000 meV and an average of 1020 meV. The lowest E_a (288 meV) was observed for the columbite Mg_{0.9}Cu_{0.1}Nb₂O_{6- δ} ,⁹² while the highest (3470 meV) was reported for the garnet Y₃Al_{4.99}Fe_{0.01}O₁₂.⁸⁹ **Fig. 2c** presents the distribution of $\log_{10} A$, with most A values lying between

1 and 10^{10} $\text{K} \cdot \text{S} \cdot \text{cm}^{-1}$ and an average of $10^{5.55} = 3.55 \times 10^5$ $\text{K} \cdot \text{S} \cdot \text{cm}^{-1}$. The lowest A ($10^{-2.05} = 8.91 \times 10^{-3}$ $\text{K} \cdot \text{S} \cdot \text{cm}^{-1}$) was observed for the columbite $\text{Mg}_{0.8}\text{Li}_{0.2}\text{Nb}_2\text{O}_{6-\delta}$,⁹² while the highest ($10^{16.0}$ $\text{K} \cdot \text{S} \cdot \text{cm}^{-1}$) was reported for the perovskite-related brownmillerite $\text{SrFeO}_{2.5+\delta}$.²⁰

We also evaluated the reproducibility of the conductivities. The conductivities of 26 oxides were reported in more than one publication, providing opportunities for cross-validation. The average standard deviations were 78.1 meV for E_a and $10^{0.41} = 2.58$ $\text{K} \cdot \text{S} \cdot \text{cm}^{-1}$ for A . Considering the distributions of A and E_a shown in **Figs. 2b** and **2c**, respectively, a high degree of consistency among independent studies is achieved despite variations in synthesis and measurement conditions.

Technical Validation

To support the reliability and scientific utility of the dataset, we performed symbolic regression analyses on both E_a and A values by using *GoodRegressor*, developed to derive analytical models that link experimental datasets with the structural and compositional features of materials. A brief summary of the program package is included in the **Supplementary Information**, whereas the technical and numerical details are provided in [Ref. 103](#).

Table 2 Structural, chemical, and physical properties of constituent elements of oxides for regression models, given as “features” for symbolic regression modeling.

Properties	Description	Unit
\bar{O}	Molar ratio of oxygen ions to metal ions	-
M	Atomic mass	$\text{g} \cdot \text{mol}^{-1}$
Z	Valence	-
r_{VI}	Shannon ionic radius with sixfold coordination to oxygen ^{104, 105}	\AA
r n_c (see below)	Shannon ionic radius depending on n_c (see below) ^{104, 105}	\AA
B	Bulk modulus	GPa
G	Shear modulus	GPa
ρ	Density	$\text{g} \cdot \text{cm}^{-3}$
ρ_{mol}	Molar density, defined as ρ/M	$\text{mol} \cdot \text{cm}^{-3}$
η_f	Ionic filling rate (per unit volume), defined as $\eta_f = N_{\text{avo}}\rho_{\text{mol}}\left(\frac{4}{3}\pi r_{\text{VI}}^3\right)$ where N_{avo} is the Avogadro’s constant	-
n	Principal quantum number of valence electrons	-
l	Azimuthal quantum number of valence electrons	-
α	Thermal expansion coefficient (linear not volumetric)	K^{-1}

κ	Thermal conductivity	$\text{W} \cdot \text{m}^{-1} \cdot \text{K}^{-1}$
$\chi - \chi_0$	Difference in electronegativity between metal ions and oxygen	-
ν	Poisson's ratio	-
θ_D	Debye temperature	K
n_c	Coordination number to oxygen ions, which depends on the occupied sites (A_s , B_s , or C_s) in different crystal classes. For example, in perovskite oxides, n_c for A_s and B_s are given as 12 and 6, respectively.	-
$\langle \dots \rangle$	Average over the constituent metal ions	Common to ...
$\sigma(\dots)$	Standard deviation over the constituent metal ions	Common to ...
$r(\dots)$	Skewness over the constituent metal ions	-

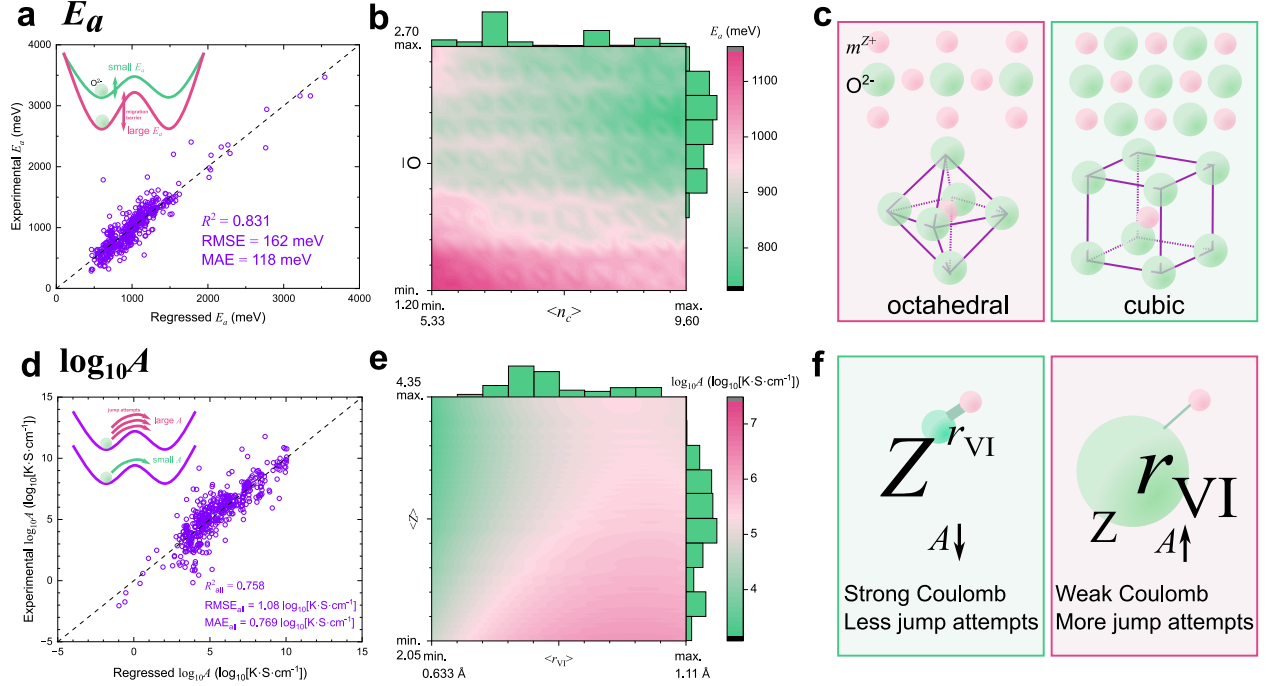


Fig. 3 Symbolic regression models governing factors of oxygen ion transport. (a) Experimental versus regressed values for the symbolic regression model for E_a , with the schematic illustrations of potential energy surfaces exhibiting low (green curve) and high E_a (pink curve). (b) Two-way partial dependence plot of the most important interaction for E_a : $\langle n_c \rangle$ - \bar{O} (see text for details). (c) Illustration of high (pink panel) and low (green panel) E_a , which depends on $\langle n_c \rangle$ and \bar{O} both. (d) Experimental versus regressed values for the symbolic regression model for $\log_{10} A$, with the schematic illustrations of potential energy surfaces with low (green arrows) and high $\log_{10} A$ (pink arrow). (e) Two-way partial dependence plot of the most important interaction for $\log_{10} A$: $\langle r_{VI} \rangle$ - $\langle Z \rangle$. (f) Illustration of how $\langle r_{VI} \rangle$ and $\langle Z \rangle$ modulate Coulombic interactions and oxygen ion jump attempts. In (b) and (e), histograms of the corresponding features for the full dataset are also shown along the upper and right axes.

As shown in **Fig. 3a**, the symbolic regression model for E_a achieved $R^2 = 0.831$, $\text{RMSE} = 162 \text{ meV}$, and $\text{MAE} = 118 \text{ meV}$ across the full dataset. The key interactions distinguishing oxides with suppressed E_a (green curve) from those with large E_a (pink curve) were identified (see Ref. 103 for details). The most important interaction was found between the average metal-oxygen

coordination number ($\langle n_c \rangle$) and the molar ratio of oxygen to metal ions (\bar{O}). Note that the most important interaction does not necessarily exclude the contribution of the other features. The two-way partial dependence plot in **Fig. 3b**, obtained by varying $\langle n_c \rangle$ and \bar{O} from the minimum to the maximum values of the full dataset while fixing other features at their mean values. As illustrated in **Fig. 3c**, a clear trend emerges: oxygen-rich environments with higher coordination numbers $\langle n_c \rangle$ (such as cubic coordination) become more favorable than oxygen-poor environments with lower $\langle n_c \rangle$ (such as octahedral or tetrahedral coordination), probably because the increased O-O repulsion in high- $\langle n_c \rangle$ configurations expands and softens the local oxygen sublattice, thereby facilitating oxygen-ion migration.

As shown in **Fig. 3d**, the symbolic regression model for $\log_{10} A$ achieved $R^2 = 0.758$, $\text{RMSE} = 10^{1.07} \text{ K} \cdot \text{S} \cdot \text{cm}^{-1}$, and $\text{MAE} = 10^{0.769} \text{ K} \cdot \text{S} \cdot \text{cm}^{-1}$ for the entire dataset. The principal interactions distinguishing low and high A values (green and pink arrows, respectively) were identified (see also Ref. 103 for details). The most important interaction involves the average Shannon ionic radius with sixfold coordination ($\langle r_{VI} \rangle$)^{104, 105} and the average metal ion valence ($\langle Z \rangle$), whose two-way dependence is shown in **Fig. 3e**. A straightforward interpretation follows; small $\langle r_{VI} \rangle$ combined with large $\langle Z \rangle$ strengthens the metal-oxygen Coulombic attraction, which stabilizes oxygen ions at their lattice sites and reduces their configurational freedom. As a result, the rate of attempted ionic jumps is suppressed. Conversely, when the metal-oxygen attraction is weaker, oxygen ions experience less localization and can attempt jumps more frequently, leading to the higher $\log_{10} A$ (**Fig. 3f**).

Our regression models can also be utilized for materials design. By substituting or doping ions and adjusting compositions, the model enables the exploration of new compounds with desirable target metrics, characterized by reduced E_a and enhanced A . In this study, the most promising candidate was identified as the apatite-type compound $\text{La}_{9.5}\text{Si}_{5.5}\text{Al}_{0.5}\text{O}_{26}$. The predicted E_a and A were 494 meV and $7.41 \times 10^6 \text{ K} \cdot \text{S} \cdot \text{cm}^{-1}$, respectively. This composition is a modified analogue of the experimentally reported apatite $\text{Nd}_{9.5}\text{Si}_{5.5}\text{Al}_{0.5}\text{O}_{26}$, which exhibited $E_a = 658 \text{ meV}$ and $A = 1.44 \times 10^7 \text{ K} \cdot \text{S} \cdot \text{cm}^{-1}$.⁷⁹ This example demonstrates the utility of the curated dataset and regression framework as a quantitative guide for both experimental and theoretical materials discovery. We envision that such data-driven predictions will accelerate the development of next-generation oxygen-ion conductors.

Associated content

Supplementary Information: Correction of the Nernst-Einstein Relation in Arrhenius Plot Analysis and A Brief Summary of Symbolic Regression Tool *GoodRegressor*

Author information

Data Availability

The total dataset created in this study is openly available at
<https://github.com/JerryGarcia1995/OxygenIonConductor>

Code Availability

The source code supporting materials prediction and design in this study is openly available at
<https://github.com/JerryGarcia1995/OxygenIonConductor>

Acknowledgments

Parts of the numerical calculations have been done using the facilities of the Supercomputer Center, the Institute for Solid State Physics, the University of Tokyo.

References

1. Singh, M., Zappa, D. & Comini, E. Solid oxide fuel cell: Decade of progress, future perspectives and challenges. *Int. J. Hydrot. Energy* **46**, 27643–27674 (2021).
2. Li, J. *et al.* Advancements in solid oxide fuel cell technology: Bridging performance gaps for enhanced environmental sustainability. *Adv. Energ. Sust. Res.* **5**, 2400132 (2024).
3. Bolvin, J. C. & Mairesse, G. Recent materials developments in fast oxide ion conductors. *Chem. Mater.* **10**, 2870–2888 (1998).
4. Kharton, V., Marques, F. & Atkinson, A. Transport properties of solid oxide electrolyte ceramics: A brief review. *Solid State Ion.* **174**, 135–149 (2004).
5. Amow, G. & Skinner, S. J. Recent developments in Ruddlesden–Popper nickelate systems for solid oxide fuel cell cathodes. *J. Solid State Electrochem.* **10**, 538–546 (2006).
6. Shen, M., Ai, F., Ma, H., Xu, H. & Zhang, Y. Progress and prospects of reversible solid oxide fuel cell materials. *iScience* **24**, 103464 (2021).
7. Yang, X., Fernández-Carrión, A. J. & Kuang, X. Oxide ion-conducting materials containing tetrahedral moieties: Structures and conduction mechanisms. *Chem. Rev.* **123**, 9356–9396 (2023).
8. Zhang, W. & Yashima, M. Recent developments in oxide ion conductors: Focusing on Dion–Jacobson phases. *Chem. Commun.* **59**, 134–152 (2023).
9. Ishihara, T., Matsuda, H. & Takita, Y. Doped LaGaO₃ perovskite type oxide as a new oxide ionic conductor. *J. Am. Chem. Soc.* **116**, 3801–3803 (1994).
10. Huang, K., Tichy, R. S. & Goodenough, J. B. Superior perovskite oxide-ion conductor; strontium- and magnesium-doped LaGaO₃: I, phase relationships and electrical properties. *J. Am. Ceram. Soc.* **81**, 2565–2575 (1998).

11. Ullmann, H., Trofimenco, N., Tietz, F., Stöver, D. & Ahamad-Khanlou, A. Correlation between thermal expansion and oxide ion transport in mixed conducting perovskite-type oxides for SOFC cathodes. *Solid State Ion.* **138**, 79–90 (2000).

12. Bucher, E., Egger, A., Ried, P., Sitte, W. & Holtappels, P. Oxygen nonstoichiometry and exchange kinetics of $\text{Ba}_{0.5}\text{Sr}_{0.5}\text{Co}_{0.8}\text{Fe}_{0.2}\text{O}_{3-\delta}$. *Solid State Ion.* **179**, 21–26 (2008).

13. Li, M. *et al.* A family of oxide ion conductors based on the ferroelectric perovskite $\text{Na}_{0.5}\text{Bi}_{0.5}\text{TiO}_3$. *Nat. Mater.* **13**, 31–35 (2014).

14. Yang, F., Zhang, H., Li, L., Reaney, I. M. & Sinclair, D. C. High ionic conductivity with low degradation in A-site strontium-doped nonstoichiometric sodium bismuth titanate perovskite. *Chem. Mater.* **28**, 5269–5273 (2016).

15. Goodenough, J. B., Ruiz-Diaz, J. E. & Zhen, Y. S. Oxide-ion conduction in Ba_2InO_5 and $\text{Ba}_3\text{In}_2\text{MO}_8$ (M=Ce, Hf, or Zr). *Solid State Ion.* **44**, 21–31 (1990).

16. Kuramochi, H., Mori, T., Yamamura, H., Kobayashi, H. & Mitamura, T. Preparation and conductivity of $\text{Ba}_2\text{In}_2\text{O}_5$ ceramics. *J. Ceram. Soc. Jpn.* **102**, 1159–1162 (1994).

17. Kurek, P., Bogusz, W., Jakubowski, W. & Krok, F. Impedance study of BIMGVOX ceramics. *Ionics* **2**, 474–477 (1996).

18. Uchimoto, Y., Yao, T., Takahi, H., Inagaki, T. & Yoshida, H. Crystal structure of $(\text{Ba}_{1-x}\text{La}_x)_2\text{In}_2\text{O}_{5+x}$ and its oxide ion conductivity. *Electrochemistry* **68**, 531–533 (2000).

19. Yao, T., Uchimoto, Y., Kinuhata, M., Inagaki, T. & Yoshida, H. Crystal structure of Ga-doped $\text{Ba}_2\text{In}_2\text{O}_5$ and its oxide ion conductivity. *Solid State Ion.* **132**, 189–198 (2000).

20. Patrakeev, M. V., Leonidov, I. A., Kozhevnikov, V. L. & Kharton, V. V. Ion–electron transport in strontium ferrites: relationships with structural features and stability. *Solid State Sci.* **6**, 907–913 (2004).

21. Shin, J. F., Oera, A., Apperley, D. C. & Slater, P. R. Oxyanion doping strategies to enhance the ionic conductivity in $\text{Ba}_2\text{In}_2\text{O}_5$. *J. Mater. Chem.* **21**, 874–879 (2011).

22. Ishihara, T. Oxide ion conductivity in defect perovskite, Pr_2NiO_4 and its application for solid oxide fuel cells. *J. Ceram. Soc. Jpn.* **122**, 179–186 (2014).

23. Fujii, K. *et al.* New perovskite-related structure family of oxide-ion conducting materials NdBaInO_4 . *Chem. Mater.* **26**, 2488–2491 (2014).

24. López, C. A., Pedregosa, J. C., Lama, D. G. & Alonso, J. A. The strongly defective double perovskite $\text{Sr}_{11}\text{Mo}_4\text{O}_{23}$: Crystal structure in relation to ionic conductivity. *J. Appl. Cryst.* **47**, 1395–1401 (2014).

25. Fujii, K. *et al.* Improved oxide-ion conductivity of NaBaInO_4 by Sr doping. *J. Mater. Chem. A* **3**, 11985–11990 (2015).

26. Fop, S. *et al.* Oxide ion conductivity in the hexagonal perovskite derivative $\text{Ba}_3\text{MoNbO}_{8.5}$. *J. Am. Chem. Soc.* **138**, 16764–16769 (2016).

27. Yang, X., Liu, S., Lu, F., Xu, J. & Kuang, X. Acceptor doping and oxygen vacancy migration in layered perovskite NdBaInO_4 -based mixed conductors. *J. Phys. Chem. C* **120**, 6416–6426 (2016).

28. Shiraiwa, M. Crystal structure and oxide-ion conductivity of $\text{Ba}_{1+x}\text{Nd}_{1-x}\text{InO}_{4-x/2}$. *J. Electrochem. Soc.* **164**, F1392–F1399 (2017).

29. McCombie K. S. *et al.* The crystal structure and electrical properties of the oxide ion conductor $\text{Ba}_3\text{WNbO}_{8.5}$. *J. Mater. Chem. A* **6**, 5290–5295 (2018).

30. Long, C. *et al.* High oxide ion conductivity in layer-structured $\text{Bi}_4\text{Ti}_3\text{O}_{12}$ -based ferroelectric ceramics. *J. Mater. Chem. C* **7**, 8825–8835 (2019).

31. Song, J., Ning, D., Boukamp, B., Bassat, J.-M. & Bouwmeester, H. J. M. Structure, electrical conductivity and oxygen transport properties of Ruddlesden–Popper phases $\text{Ln}_{n+1}\text{Ni}_n\text{O}_{3n+1}$ ($\text{Ln} = \text{La, Pr and Nd}$; $n = 1, 2$ and 3). *J. Mater. Chem. A* **8**, 22206–22221 (2020).

32. Fop, S. *et al.* High oxide ion and proton conductivity in a disordered hexagonal perovskite. *Nat. Mater.* **19**, 752–757 (2020).

33. Zhang, W. *et al.* Oxide-ion conduction in the Dion–Jacobson phase $\text{CsBi}_2\text{Ti}_2\text{NbO}_{10-\delta}$. *Nat. Commun.* **11**, 1224 (2020).

34. Fop, S., McCombie, K., Smith, R. I. & McLaughlin A. C. Enhanced oxygen ion conductivity and mechanistic understanding in $\text{Ba}_3\text{Nb}_{1-x}\text{V}_x\text{MoO}_{8.5}$. *Chem. Mater.* **32**, 4724–4733 (2020).

35. Gilane, A. Fop, S., Sher, F., Smith, R. I. & McLaughlin, A. C. The relationship between oxide-ion conductivity and cation vacancy order in the hybrid hexagonal perovskite $\text{Ba}_3\text{VWO}_{8.5}$. *J. Mater. Chem. A* **8**, 16506–16514 (2020).

36. Yashima, M. *et al.* High oxide-ion conductivity through the interstitial oxygen site in $\text{Ba}_7\text{Nb}_4\text{MoO}_{20}$ -based hexagonal perovskite related oxides. *Nat. Commun.* **12**, 556 (2021).

37. Sakuda, Y., Hester, J. R. & Yashima, M. Improved oxide-ion and lower proton conduction of hexagonal perovskite-related oxides based on $\text{Ba}_7\text{Nb}_4\text{MoO}_{20}$ by Cr^{6+} doping. *J. Ceram. Soc. Jpn.* **130**, 442–447 (2022).

38. Murakami, T. *et al.* High oxide-ion conductivity in a hexagonal perovskite-related oxide $\text{Ba}_7\text{Ta}_{3.7}\text{Mo}_{1.3}\text{O}_{20.15}$ with cation site preference and interstitial oxide ions. *Small* **18**, 2106785 (2022).

39. Strickler, D. W. & Carlson, W. G. Electrical conductivity in the ZrO_2 -rich region of several M_2O_3 – ZrO_2 systems. *J. Am. Ceram. Soc.* **48**, 286–289 (1965).

40. Tuller, H. L. & Nowick, A. S. Doped ceria as a solid oxide electrolyte. *J. Electrochem. Soc.* **122**, 255–259 (1975).

41. Miyayama, M., Nishi, T. & Yanagida, H. Oxygen ionic conduction in Y_2O_3 -stabilized Bi_2O_3 and ZrO_2 composites. *J. Mater. Sci.* **22**, 2624–2628 (1987).

42. Yahiro, H., Eguchi, Y., Eguchi, K. & Arai, H. Oxygen ion conductivity of the ceria-samarium oxide system with fluorite structure. *J. Appl. Electrochem.* **18**, 527–531 (1988).

43. Mori, M. *et al.* Cubic-stabilized zirconia and alumina composites as electrolytes in planar type solid oxide fuel cells. *Solid State Ion.* **74**, 157–164 (1994).

44. Steele, B. C. H. Appraisal of $\text{Ce}_{1-y}\text{Gd}_y\text{O}_{2-y/2}$ electrolytes for IT-SOFC operation at 500°C. *Solid State Ion.* **129**, 95–110 (2000).

45. Kharton V. V. *et al.* Ceria-based materials for solid oxide fuel cells. *J. Mater. Sci.* **36**, 1105–1117 (2001).

46. Takahashi, T., Iwahara, H. & Arao, T. High oxide ion conduction in sintered oxides of the system Bi_2O_3 - Y_2O_3 . *J. Appl. Electrochem.* **5**, 187–195 (1975).

47. Takahashi, T. & Iawahara, H. Oxide ion conductors based on bismuthsesquioxide. *Mat. Res. Bull.* **13**, 1447–1453 (1978).

48. Verkerk, M. J., Keizer, K. & Burggraaf, A. J. High oxygen ion conduction in sintered oxides of the Bi_2O_3 - Er_2O_3 system. *J. Appl. Electrochem.* **10**, 81–90 (1980).

49. Verkerk, M. J. & Burggraaf, A. J. High oxygen ion conduction in sintered oxides of the Bi_2O_3 - Ln_2O_3 system. *Solid State Ion.* **3–4**, 463–467 (1981).

50. Benkaddour, M., Obbade, S., Conflant, P. & Drache, M. $\text{Bi}_{0.85}\text{Ln}_{0.15(1-n)}\text{V}_{0.15n}\text{O}_{1.5+0.15n}$ fluorite type oxide conductors: Stability, conductivity, and powder crystal structure investigations. *J. Solid State Chem.* **163**, 300–307 (2002).

51. Punn, R., Feteira, A. M., Sinclair, D. C. & Greaves, C. Enhanced oxide ion conductivity in stabilized δ - Bi_2O_3 . *J. Am. Chem. Soc.* **128**, 15386–15387 (2006).

52. Jung, D. W., Duncan, K. L. & Wachsman, E. D. Effect of total dopant concentration and dopant ratio on conductivity of $(\text{DyO}_{1.5})_x-(\text{WO}_3)_y-(\text{BiO}_{1.5})_{1-x-y}$. *Acta Mater.* **58**, 355–363 (2010).

53. Kunag, X., Payne, J. L., Johnson, M. R. & Evans, I. R. Remarkably high oxide ion conductivity at low temperature in an ordered fluorite-type superstructure. *Angew. Chem.* **51**, 690–694 (2012).

54. Karmalkar, D. N. *et al.* Enhanced phase stability and oxide-ion conductivity in V- and Sr/Ca-codoped Bi_2O_3 ceramics. *J. Phys. Chem. C* **129**, 107–120 (2024).

55. Abraham, F., Boivin, J. C., Mairesse, G. & Nowogrocki, G. The bimevox series: A new family of high performances oxide ion conductors. *Solid State Ion.* **40–41**, 934–937 (1990).

56. Sharma, V., Shukla, A. K. & Gopalakrishnan, J. Effect of aliovalent-cation substitution on the oxygen-ion conductivity of $\text{Bi}_4\text{V}_2\text{O}_{11}$. *Solid State Ion.* **58**, 359–362 (1992).

57. Yan, J. & Greenblatt, M. Ion conductivities of $\text{Bi}_4\text{V}_{2-x}\text{M}_x\text{O}_{11-x2}$ ($\text{M}=\text{Ti, Zr, Sn, Pb}$) solid solutions. *Solid State Ion.* **81**, 225–233 (1995).

58. Kim, S.-K. & Miyayama, M. Anisotropy in oxide ion conductivity of $\text{Bi}_4\text{V}_{2-x}\text{Co}_x\text{O}_{11-\delta}$. *Solid State Ion.* **104**, 295–302 (1997).

59. Yaremchenko, A. A. *et al.* Structure and electronic conductivity of $\text{Bi}_{2-x}\text{La}_x\text{V}_{0.9}\text{Cu}_{0.1}\text{O}_{5.5-\delta}$. *Mater. Chem. Phys.* **77**, 552–558 (2003).

60. Bonanos, N. High oxide ion conductivity in bismuth uranate, Bi_2UO_6 . *Mat. Res. Bull.* **24**, 1531–1540 (1989).

61. Esaka, T., Mina-ai, T. & Iwahara, H. Oxide ion conduction in the solid solution based on the scheelite-type oxide PbWO_4 . *Solid State Ion.* **57**, 319–325 (1992).

62. Esaka, T., Tachibana, R. & Takai, S. Oxide ion conduction in the Sm-substituted PbWO_4 phases. *Solid State Ion.* **92**, 129–133 (1996).

63. Cheng, J., Liu, C., Cao, W., Qi, M. & Shao, G. Synthesis and electrical properties of scheelite $\text{Ca}_{1-x}\text{Sm}_x\text{MoO}_{4+\delta}$ solid electrolyte ceramics. *Mat. Res. Bull.* **46**, 185–189 (2011).

64. Li, C., Bayliss, R. D. & Skinner, S. J. Crystal structure and potential interstitial oxide ion conductivity of LnNbO_4 and $\text{LnNb}_{0.92}\text{W}_{0.08}\text{O}_{4.04}$ ($\text{Ln}=\text{La, Pr, Nd}$). *Solid State Ion.* **262**, 530–535 (2014).

65. Takai, S. *et al.* Electrochemical properties of Cs-substituted CaWO_4 and BaWO_4 oxide ion conductors. *J. Ceram. Soc. Japan* **124**, 819–822 (2016).

66. Cheng, J. & He, J. Electrical properties of scheelite structure ceramic electrolytes for solid oxide fuel cells. *Mater. Lett.* **209**, 525–527 (2017).

67. Yang, X. *et al.* Cooperative mechanisms of oxygen vacancy stabilization and migration in the isolated tetrahedral anion Scheelite structure. *Nat. Commun.* **9**, 4484 (2018).

68. Kawaguchi, R., Akizawa, R., Shan, Y. J., Tezuka, K. & Katsumata, T. Synthesis and examination of $\text{GdNb}_{1-x}\text{W}_x\text{O}_{4+\delta}$ new scheelite-type oxide-ion conductor. *Solid State Ion.* **355**, 115415 (2020).

69. Auckett, J. E., Lopez-Odriozola, L., Clark, S. J. & Evans, I. R. Exploring the nature of the fergusonite–scheelite phase transition and ionic conductivity enhancement by Mo^{6+} doping in LaNbO_4 . *J. Mater. Chem. A* **9**, 4091–4102 (2021).

70. Yang, X. *et al.* Oxide-ion conductivity optimization in BiVO_4 scheelite by an acceptor doping strategy. *Inorg. Chem. Front.* **9**, 2644–2658 (2022).

71. Shan, Y. J., Kawaguchi, R., Akizawa, R. & Tezuka, K. Crystal structure and ionic conductivity of novel rare-earth niobates LnNbO_4 ($\text{Ln} = \text{Nd, Sm, Eu, Gd}$) by substituting Nb with W. *Ionics* **29**, 2697–2703 (2023).

72. Mullens, B. G. *et al.* Variable temperature *in situ* neutron powder diffraction and conductivity studies of undoped HoNbO_4 and HoTaO_4 . *Chem. Mater.* **36**, 5002–5016 (2024).

73. Nakayama S., Kageyama, T., Aono, H. & Sadaoka, Y. Ionic conductivity of lanthanoid silicates, $\text{Ln}_{10}(\text{SiO}_4)_6\text{O}_3$ ($\text{Ln} = \text{La, Nd, Sm, Gd, Dy, Y, Ho, Er and Yb}$). *J. Mater. Chem.* **5**, 1801–1805 (1995).

74. Abram, E. J., Sinclair, D. C. & West, A. R. A novel enhancement of ionic conductivity in the cation-deficient apatite $\text{La}_{9.33}(\text{SiO}_4)_6\text{O}_2$. *J. Mater. Chem.* **11**, 1978–1979 (2001).

75. Shaula, A. L., Kharton, V. V. & Marques, F. M. B. Oxygen ionic and electronic transport in apatite-type $\text{La}_{10-x}(\text{Si,Al})_6\text{O}_{26\pm\delta}$. *J. Solid State Chem.* **178**, 2050–2061 (2005).

76. Leon-Reina, L. *et al.* High oxide ion conductivity in Al-doped germanium oxyapatite. *Chem. Mater.* **17**, 596–600 (2005).

77. Masabuchi, U., Higuchi, M., Takeda, T. & Kikkawa, S. Oxide ion conduction mechanism in $\text{RE}_{9.33}(\text{SiO}_4)_6\text{O}_2$ and $\text{Sr}_2\text{RE}_8(\text{SiO}_4)_6\text{O}_2$ (RE = La, Nd) from neutron powder diffraction. *Solid State Ion.* **177**, 263–268 (2006).

78. Yoshioka, H. Enhancement of ionic conductivity of apatite-type lanthanum silicates doped with cations. *J. Am. Ceram. Soc.* **90**, 3099–3105 (2007).

79. An, T. *et al.* Crystallographic correlations with anisotropic oxide ion conduction in aluminum-doped neodymium silicate apatite electrolytes. *Chem. Mater.* **25**, 1109–1120 (2013).

80. Arikawa, H., Nishigchi, H., Ishihara, T. & Takita Y. Oxide ion conductivity in Sr-doped $\text{La}_{10}\text{Ge}_6\text{O}_{27}$ apatite oxide. *Solid State Ion.* **136–137**, 31–37 (2000).

81. Wei, T., Xu, J. & Zhu, W. New apatite-type oxide ion conductors $\text{Ce}_{9.33+x}\text{Si}_6\text{O}_{26+\delta}$: Structures, phase stabilities, electrical properties, and conducting mechanisms. *Energy Sci. Eng.* **10**, 525–537 (2022).

82. Martin-Sedeño, M. C. *et al.* Enhancement of Oxide Ion Conductivity in Cuspidine-Type Materials. *Chem. Mater.* **16**, 4960–4968 (2004).

83. Chesnaud, A. *et al.* Cuspidine-like compounds $\text{Ln}_4[\text{Ga}_{2(1-x)}\text{Ge}_{2x}\text{O}_{7+x}\square_{1-x}]\text{O}_2$ (Ln = La, Nd, Gd; $x \leq 0.4$). *Chem. Mater.* **16**, 5372–5379 (2004).

84. Martin-Sedeño, M. C. *et al.* Structural and electrical investigation of oxide ion and proton conducting titanium cuspidines. *Chem. Mater.* **17**, 5989–5998 (2005).

85. Thomas, C. I. *et al.* Phase stability control of interstitial oxide ion conductivity in the $\text{La}_{1+x}\text{Sr}_{1-x}\text{Ga}_3\text{O}_{7+x/2}$ melilite family. *Chem. Mater.* **22**, 2510–2516 (2010).

86. Diaz-Lopez, M. *et al.* Interstitial Oxide Ion Conductivity in the Langasite Structure: Carrier Trapping by Formation of $(\text{Ga,Ge})_2\text{O}_8$ Units in $\text{La}_3\text{Ga}_{5-x}\text{Ge}_{1+x}\text{O}_{14+x/2}$ ($0 < x \leq 1.5$). *Chem. Mater.* **15**, 5742–5758 (2019).

87. Li, X. *et al.* B-site mixed cationic tetrahedral layer confined the concentration and mobility of interstitial oxygen in mellite family. *J. Mater. Chem. A* **11**, 5615–5626 (2023).

88. Bazzaoui, H. *et al.* La Substitution into the Melilite Derivative $\text{Ca}_5\text{Ga}_6\text{O}_{14}$: Prediction, Synthesis and Ionic Conductivity. *Inorg. Chem.* **63**, 18902–18913 (2024).

89. Rotman, S. R. & Tuller, H. L. Defect-property correlations in garnet crystals. *VII: The electrical conductivity and defect structure of yttrium aluminum and yttrium iron garnet solid solutions. *J. Electroceram.* **2**, 95–104 (1998).

90. Kharton, V. V. *et al.*, Ionic transport in $\text{Gd}_3\text{Fe}_5\text{O}_{12}$ - and $\text{Y}_3\text{Fe}_5\text{O}_{12}$ -based garnets. *J. Electrochem. Soc.* **150**, J33–J42 (2003).

91. Kramer, S. A. & Tuller, H. L. A novel titanate-based oxygen ion conductor: $\text{Gd}_2\text{Ti}_2\text{O}_7$. *Solid State Ion.* **82**, 25–23 (1995).

92. Morkhova, Y. A. *et al.* Magnocolumbites $\text{Mg}_{1-x}M_x\text{Nb}_2\text{O}_{6-\delta}$ ($x = 0, 0.1$, and 0.2 ; $M = \text{Li}$ and Cu) as new oxygen ion conductors: Theoretical assessment and experiment. *J. Phys. Chem. C* **127**, 52–58 (2023).

93. Singh, P. & Goodenough, J. B. $\text{Sr}_{1-x}\text{K}_x\text{Si}_{1-y}\text{Ge}_y\text{O}_{3-0.5x}$: A new family of superior oxide-ion conductors. *Energy Environ. Sci.* **5**, 9626–9631 (2012).

94. Singh, P. & Goodenough, J. B. Monoclinic $\text{Sr}_{1-x}\text{Na}_x\text{SiO}_{3-0.5x}$: New superior oxide ion electrolytes. *J. Am. Chem. Soc.* **135**, 10149–10154 (2013).

95. Wei, T. *et al.* $\text{Sr}_{3-3x}\text{Na}_{3x}\text{Si}_3\text{O}_{9-1.5x}$ ($x = 0.45$) as a superior solid oxide-ion electrolyte for intermediate temperature-solid oxide fuel cells. *Energy Sci. Eng.* **7**, 1680–1684 (2014).

96. Tealdi, C. *et al.* Nature of conductivity in SrSiO_3 -based fast ion conductors. *Chem. Commun.* **50**, 14732–14735 (2014).

97. Unke, O. T. *et al.* Machine learning force fields. *Chem. Rev.* **121**, 10142–10186 (2021).

98. Wang, G. *et al.* Machine learning interatomic potential: Bridge the gap between small-scale models and realistic device-scale simulations. *iScience* **27**, 109673 (2024).

99. Xia, J., Zhang, Y. & Jiang, B. The evolution of machine learning potentials for molecules, reactions and materials. *Chem. Soc. Rev.* **54**, 4790–4821 (2025).

100. *Web of Science* <https://www.webofscience.com/wos/woscc/smart-search> (2025).
101. *Scopus* <https://www.elsevier.com/products/scopus> (2025).
102. *Google Scholar* <https://scholar.google.com/> (2025).
103. Shannon, R. D. Revised effective ionic radii and systematic studies of interatomic distances in halides and chalcogenides. *Acta Crystallogr. A* **32**, 751–767 (1976).
104. Baloch, A. A. B. *et al.* Extending Shannon's ionic radii database using machine learning. *Phys. Rev. Materials* **5**, 043804 (2021).
105. Jang, S.-H. *GoodRegressor*: A general-purpose symbolic regression framework for physically interpretable materials modeling. Preprint at <https://doi.org/10.48550/arXiv.2510.18325> (2025).

Supplementary Information

Charting the Landscape of Oxygen Ion Conductors: A 60-Year Dataset with Interpretable Regression Models

*Seong-Hoon Jang^{*1}, Shin Kiyohara¹, Hitoshi Takamura², Yu Kumagai^{**1,3}*

¹ *Institute for Materials Research, Tohoku University, 2-1-1 Katahira, Aoba-ku, Sendai 980-8577, Japan.*

² *Department of Materials Science, Graduate School of Engineering, Tohoku University, 6-6-02 Aramaki, Aoba-ku, Sendai 980-8579, Japan*

³ *Organization for Advanced Studies, Tohoku University, 2-1-1 Katahira, Aoba-ku, Sendai 980-8577, Japan*

*Corresponding authors:

jang.seonghoon.b4@tohoku.ac.jp (S.-H. Jang)

yukumagai@tohoku.ac.jp (Y. Kumagai)

This file contains:

- Correction of the Nernst-Einstein Relation in Arrhenius Plot Analysis

Correction of the Nernst-Einstein Relation in Arrhenius Plot Analysis

A common issue in the literature involves the use of an incorrect form of the Nernst-Einstein equation when constructing Arrhenius plots. The correct relationship is given by

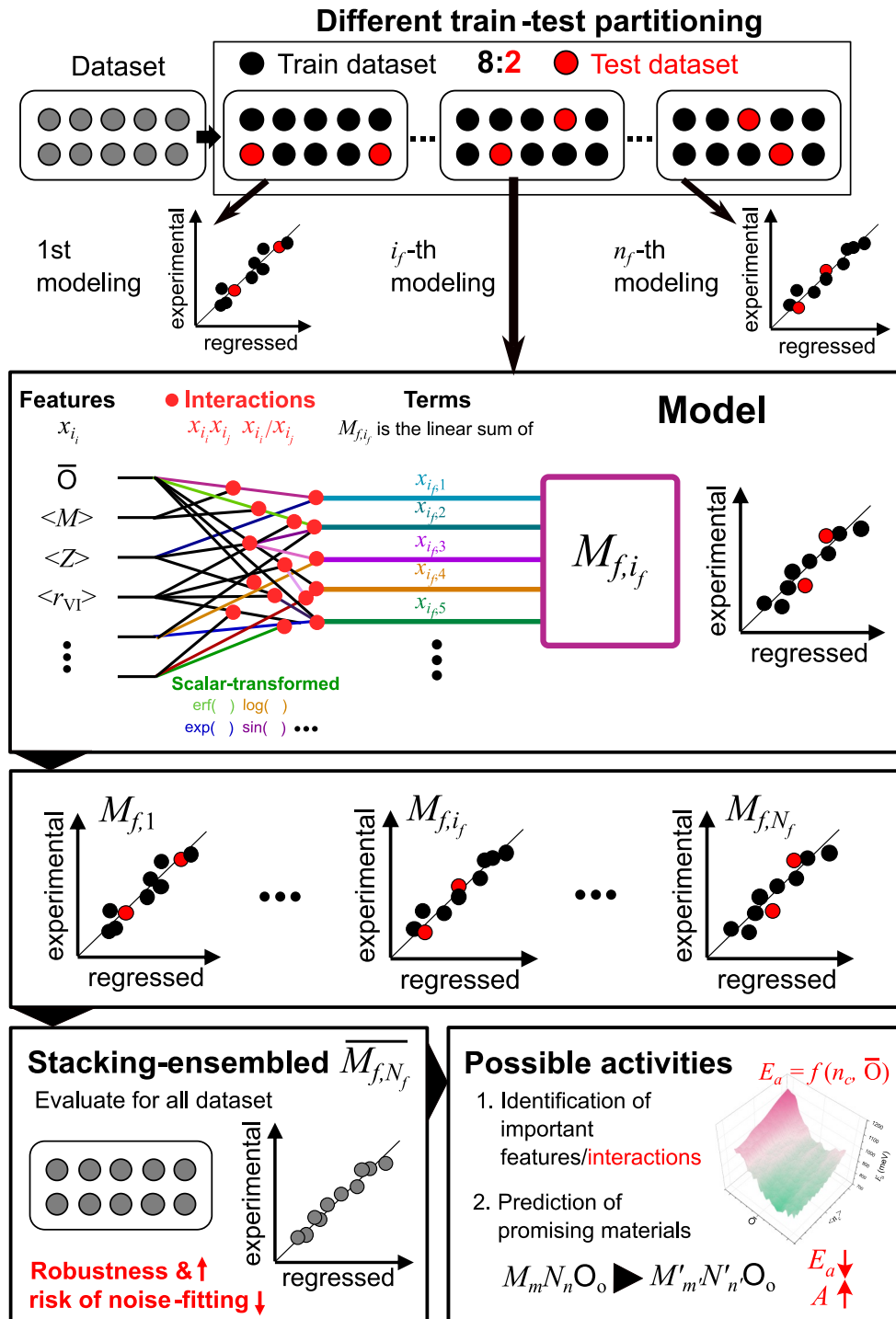
$$\sigma_T T = A \exp\left(-\frac{E_a}{RT}\right), \quad (S1)$$

where R is the gas constant. However, many studies instead employ the simplified form

$$\sigma_T = A \exp\left(-\frac{E_a}{RT}\right). \quad (S2)$$

This inconsistency leads to systematic errors in the calculated values of E_a and A . For instance, in an experimental study on $\text{Ce}_{9.33+x}\text{Si}_6\text{O}_{26+\delta}$, the incorrect expression yielded $E_a = 0.95, 0.97$, and 0.96 eV for $x = 0.43, 0.67$, and 1.03 , respectively (see Fig. 7 in that paper).¹ Upon manually re-curating the Arrhenius data using the correct form, the corresponding activation energies were found to be $E_a = 0.92, 0.93$, and 0.92 eV. Thus, the incorrect formulation systematically overestimates E_a by approximately $0.03\sim0.04$ eV. Although such deviations may appear minor relative to the magnitude of E_a , they can nonetheless compromise the accuracy of datasets and hinder reliable model development. Therefore, careful attention to the correct equation form is warranted.

A Brief Summary of Symbolic Regression Tool *GoodRegressor*



Supplementary Fig. 1 Workflow of the symbolic regression used in this study. Starting from the experimental dataset, the program performs multiple train-test partitions (8: 2 ratio, repeated ten

times) to construct stacking-ensembled symbolic regression models.³ In each iteration, feature interactions (e.g., multiplications $x_{i_i}x_{i_j}$ and divisions x_{i_i}/x_{i_j}) and scalar transformations (e.g., $\text{erf}(x_{i_i})$, $\log(x_{i_i})$, $\exp(x_{i_i})$, $\sin(x_{i_i})$, $\sqrt{x_{i_i}}$, $x_{i_i}^2$, \dots) are explored to maximize the coefficient of determination (R_{test}^2) of the test dataset. The resulting models are stacking-ensembled to yield a robust and interpretable expression that mitigates overfitting. By analyzing the frequency of an interaction and the magnitude of its z-scored coefficients across the ensembles, the program identifies key physical descriptors governing the target property and enables the virtual design of promising material candidates through compositional modulation.

In *GoodRegressor* as illustrated in **Supplementary Fig. 1**, starting from the experimental dataset, the program performs random train-test partitions with a user-defined ratio (8: 2 in this study) to build symbolic regression models.² This process is repeated n_f times (10 times in this study) using different randomly sampled training datasets of the same size drawn from the full dataset, thereby enabling “bagging”. In the i_f -th modeling iteration ($1 \leq i_f \leq n_f$), beginning with the feature set x_{i_i} listed in **Table 2 in the main text**, the program optimizes not only their multiple interactions (e.g., multiplications $x_{i_i}x_{i_j}$ and divisions x_{i_i}/x_{i_j}) but also scalar transformations (e.g., $\text{erf}(x_{i_i})$, $\log(x_{i_i})$, $\exp(x_{i_i})$, $\sin(x_{i_i})$, $\sqrt{x_{i_i}}$, $x_{i_i}^2$, \dots) to maximize the coefficient of determination (R_{test}^2) of the test dataset based on the regression model trained on the training subset. The resulting symbolic regression model M_{f,i_f} is expressed as a linear combination of terms $(x_{i_f,1}, x_{i_f,2}, \dots)$, each corresponding to a feature, an interaction, or their scalar-transforms (often complicated algebraically). Finally, all iteration models $(M_{1,i_f}, \dots, M_{f,i_f}, \dots, M_{f,N_f})$ are stacking-ensembled to

yield the final model $\overline{M_{f,n_f}}$. Increasing n_f enhances model robustness, reflected in higher R^2 values for predictions across the entire dataset, and mitigates the risk of noise-fitting that could otherwise lead to overfitting on unseen data. On top of this, from the ensemble of models $\{M_{1,i_f}, \dots, M_{f,i_f}, \dots, M_{f,n_f}\}$, both important individual features and key “interactions” can be identified by evaluating their frequency of occurrence and average coefficient magnitudes across models. Roughly, the former answers to “how many models do have term(s) where target features, x_{i_l}, x_{i_j}, \dots , coexist (interact)?”, while the latter answers to “what is the total average of the absolute values of z-scored coefficients for term(s) where target features, x_{i_l}, x_{i_j}, \dots , coexist (interact)?”. Moreover, the stacking-ensembled $\overline{M_{f,n_f}}$ can be used to predict promising material candidates with desired target properties by virtually substituting or doping atoms (ions) within existing compositions in the experimental dataset.

Supplementary Reference

1. Wei, T., Xu, J. & Zhu, W. New apatite-type oxide ion conductors $\text{Ce}_{9.33+x}\text{Si}_6\text{O}_{26+\delta}$: Structures, phase stabilities, electrical properties, and conducting mechanisms. *Energy Sci. Eng.* **10**, 525–537 (2022).
2. Jang, S.-H. *GoodRegressor*: A general-purpose symbolic regression framework for physically interpretable materials modeling. Preprint at <https://doi.org/10.48550/arXiv.2510.18325> (2025).